Dynamic observation of manganese adatom mobility at perovskite oxide catalyst interfaces with water

Gaurav Lole[1,2], Vladimir Roddatis[1,7], Ulrich Ross [1], Marcel Risch [1,3], Tobias Meyer [4], Lukas Rump [4,5], Janis Geppert [1], Garlef Wartner [1,8], Peter Blöchl [5,6] & Christian Jooss [1,2✉]

Real time in-situ microscopy imaging of surface structure and atom dynamics of heterogeneous catalysts is an important step for understanding reaction mechanisms. Here, using in-situ environmental transmission electron microscopy (ETEM), we directly visualize surface atom dynamics at manganite perovskite catalyst surfaces for oxygen evolution reaction (OER), which are ≥ 20 times faster in water than in other ambients. Comparing (001) surfaces of $La_{0.6}Sr_{0.4}MnO_3$ and $Pr_{0.67}Ca_{0.33}MnO_3$ with similar initial manganese valence state and OER activity, but very different OER stability, allows us to distinguish between reversible surface adatom dynamics and irreversible surface defect chemical reactions. We observe enhanced reversible manganese adatom dynamics due to partial solvation in adsorbed water for the highly active and stable $La_{0.6}Sr_{0.4}MnO_3$ system, suggesting that aspects of homogeneous catalysis must be included for understanding the OER mechanism in heterogeneous catalysis.

[1] Institute of Materials Physics, University of Goettingen, Friedrich-Hund-Platz 1, 37077 Goettingen, Germany. [2] International Center for Advanced Studies of Energy Conversion (ICASEC), University of Goettingen, D-37077 Goettingen, Germany. [3] Helmholtz-Zentrum Berlin für Materialien und Energie GmbH, Young Investigator Group Oxygen Evolution Mechanism Engineering, 14109 Berlin, Germany. [4] 4th Physical Institute, Solids and Nanostructures, University of Goettingen, Friedrich-Hund-Platz 1, 37077 Goettingen, Germany. [5] Institute for Theoretical Physics, University of Goettingen, Friedrich-Hund-Platz 1, 37077 Goettingen, Germany. [6] Institute for Theoretical Physics, Clausthal University of Technology, Leibnizstr. 10., D-38678 Clausthal-Zellerfeld, Germany. [7] Present address: Helmholtz-Zentrum Potsdam Deutsches GeoForschungsZentrum GFZ, Telegrafenberg 14473, Potsdam, Germany. [8] Present address: Helmholtz-Zentrum Berlin für Materialien und Energie GmbH, Young Investigator Group Operando Interface-Photochemistry, 12489 Berlin, Germany. ✉email: cjooss@gwdg.de

The efficiency of electrochemical water splitting for the sustainable production of clean fuels from renewable energy sources is limited by a large overpotential of the anodic oxygen evolution reaction (OER)[1–3]. Understanding of its origin requires knowledge about the pathway of the formation of di-oxygen O_2 out of 2 H_2O molecules by a proton-coupled electron transfer. Even for the best electrocatalysts, i.e., transition metal (M) oxides (O), the reaction path for O–O formation is not well understood. For heterogeneous systems, the reaction is catalyzed at active surface sites, where different sites and mechanisms are suggested. This includes single[4] or dual[5–7] transition metal (M) sites with flexible valence states, concerted proton–electron transfer[8,9] as well as redox active lattice O[10–12], including oxygen vacancy formation and annihilation[13]. Despite remarkable progress in application of density functional theory (DFT) to the oxide-water interface, the theoretical understanding of the dynamic interface structure during OER is still limited since it requires serious approximations[14]. Among of the far-reaching are the frozen surface approximation and that solvation effects are, if at all, only considered as a static average. This underestimates the flexibility of M surface coordination due to interface solvent effects that is on the other hand known to be crucial in homogeneous catalysis for the formation of high- or hetero-valent M–O moieties that precede O–O bond formation[15]. There are controversial conclusions whether the predicted unsuitable scaling relation between metal M–OH and M–O adsorption energies[9,16,17] as the origin of large overpotentials for single surface sites can be broken by bifunctional mechanism at two distinct M and M' sites[18] or is restored by surface solvation[19]. Recent experiments show that ternary alloying of two different transition metals with a highly flexible coordination metals indeed lead to a remarkable reduction of OER overpotential in gelled oxyhydroxides[20]. An improved theoretical understanding thus requires a comprehensive atomic scale understanding of the dynamic electrolyte-catalyst interface structure under OER conditions as an essential ingredient for the knowledge driven further improvement of electrocatalysts by material design.

In addition to OER activity, the stability is strongly affected by the interfacial electrolyte interactions. A distinction between reversible dynamics that emerges in a stationary state and irreversible processes that change the activity is essential. Such insights are promoted by the progress of operando studies that can address different types of dynamical changes. A first type of rather slow dynamics is the change of electrode surface during potential cycling. The important role of solvate interactions has been e.g., established for the noble metal Pt, where Pt surface oxide that is formed under anodic polarization adsorbs water that dissociates and forms hydrated Pt[21]. Metal oxides such as CoO_x can form a disordered surface during OER[22,23]. A second type of rather fast dynamics is due to thermally activated mobility of surface atoms[24] or adatoms[25] that is hardly accessible in operando experiments. Clearly, surface adatom dynamics depends on temperature and surface barriers that can be modified due to H_2O solvation or dissociation[26] and is always present, even in thermal equilibrium. Driving the OER, the emerging non-equilibrium surface should show a reversible dynamics in a stationary state that depends on the formed atomic and chemical surface structure. Non-equilibrium dynamics of catalyst atoms may be even involved in OER mechanism[27]. A third type of surface dynamics is irreversible defect reactions, typically the formation of oxygen vacancies[13,28] or the dissolution of metallic species[29]. Such processes are even gradually present at the highest performance system RuO_2[30]. Metal dissolution can depend on overpotential[31,32] surface symmetry[33], pH value and particle size[34]. In order to avoid such corrosive processes, approaches for self-repair have been pursued[35]. Despite a huge progress in

application of different operando techniques[36], comprehensive atomic scale understanding of all three classes of surface dynamics are far of reach at present, but are urgently required to establish the intimate connections between surface stability, the nature of the active sites and reaction pathways[37].

In situ environmental transmission electron microscopy (ETEM) in combination with aberration correction and image simulation has developed to a level where it can provide atomic resolution real space information about the equilibrium surface reconstruction in various ambient conditions[38–40] including strategies for controlling the impact of electron beam[41,42]. The recent development of atomic scale dynamic studies show surface mobility of Ce atoms on CeO_2 facets in high vacuum[43] and a transition of a TiO_2 surface reconstruction in H_2O from static to dynamic after adding CO[44]. Steps towards the control of electron beam-induced and applied electric potentials at TEM samples enable in situ studies of electrode surfaces in ETEM under anodic polarization, approaching OER relevant potentials[28,45].

In this study, two perovskite manganites $AMnO_3$ were selected, where the Mn valence state can be controlled by A-site doping without changing the crystal symmetry. Specifically, $La_{1-x}Sr_xMnO_3$ at $x = 0.4$ (LSMO) is a metal-like electrode with high and stable oxygen evolution activity that is close to IrO_2[29]. Moreover, $Pr_{1-x}Ca_xMnO_3$ at $x = 0.33$ (PCMO) is a semi-conducting small polaron material with high initial OER activity, yet less stability, due to oxygen vacancy formation and fast leaching of the resulting reduced Mn species. Thus LSMO is suitable for the study of reversible surface dynamics, whereas PCMO shows a pronounced irreversible defect reaction. Both systems have almost the same initial Mn valence but differ in Mn–O covalency and charge localization. This differences allows us to correlate in situ ETEM studies of surface structure and dynamics with ex situ analysis of electrochemical OER. We find that the (001) surfaces of both manganites show an at least 20 times higher Mn-adatom mobility in an adsorbed water layer compared to other ambients.

Results and discussion

Structure, activity, and stability of LSMO and PCMO (001). Rotating ring disk electrode (RRDE) cyclovoltammetry (CV) was carried out at epitaxial (001) oriented thin film electrodes in 0.1 M aqueous KOH solution (Fig. 1). Both materials initially show good electrocatalytic oxygen evolution performance (for oxygen detection and Tafel analysis see Supplementary Figs. 1–3). Most striking is the different behavior just below the onset of the OER, where a redox wave is visible in PCMO as a negative current peak at $E = 1.3$ V vers reversible hydrogen electrode (RHE), complemented by a positive shoulder at the onset of OER. This feature is absent in LSMO. The redox couple is related to reversible formation and annihilation of oxygen vacancies, which are electron donors and thus induce a surface reduction of the transition metal[13]. The defect reaction is given by

$$Pr_{1-x}Ca_xMn^{2+x}O_{2.5} + V_o^{\cdot\cdot} + 1/2O_2 \gtrless Pr_{1-x}Ca_xMn^{3+x}O_3 + 2e^-$$
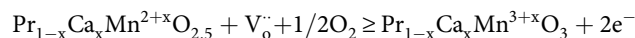
For neutral pH values in an unbuffered solution, which is more relevant for the comparison to in situ XANES and ETEM studies, a similar behavior of the CV is observed[13]. The easy formation of $V_o^{\cdot\cdot}$ in PCMO indicates that lattice oxygen is redox active, such that transfer of holes between Mn3d and O2p states can oxidize O^{2-} to form O^- and $O_2(g)$; see e.g., refs. [46,47]. For LSMO such a surface redox process is only observed when the cycling is extended to more negative potentials below $E = 0.6$ V vers RHE[48].

Comparing the cycle dependence of the OER activity for LSMO and PCMO in Fig. 1b, there is a strong difference in
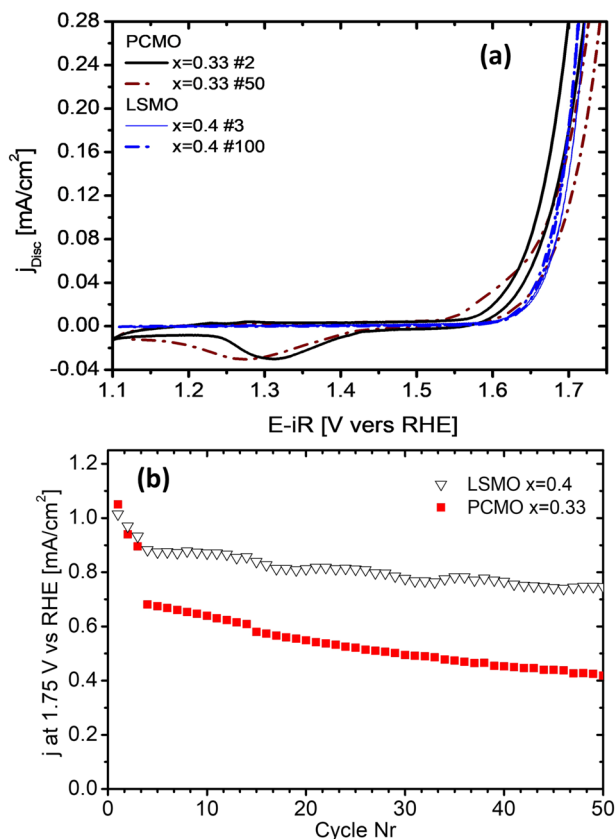
Fig. 1 Electrocatalytic characterization. a Cyclovoltammetry of (001) oriented epitaxial thin film manganite electrodes in 0.1 M aqueous KOH solution at 10 mV/s and rotated at 1600 rpm for cycles #2/#50 (PCMO) and #3/#100 (LSMO), respectively. In addition to the OER, PCMO shows a pronounced surface redox couple. **b** Temporal stability of the electrode current density at $E = 1.75$ V vers. RHE for cycling from $E = 1.1$–1.75 V vers. RHE and 7 min chronoamperometric OER between cycle 3 and 4 (see method section).

stability between both electrodes. Initially, the current density j of both systems at $E = 1.75$ V vers. RHE is similar, i.e., $j = 1.03$ mA/cm^2 for LSMO and $j = 1.05$ mA/cm^2 for PCMO. These values are close to the activity of IrO$_2$ (110) films[49]. However, upon cycling and chronoamperometric OER between cycle 3 and 4, the decrease for PCMO is much more pronounced than for LSMO. Comparing the pristine and post electrolysis structure of LSMO and PCMO after 50 electrochemical cycles (Supplementary Figs. 4–7) reveals significant differences. Whereas for LSMO the crystalline surface structure with flat terraces and unit cell height steps is fully preserved, PCMO displays an increase of surface roughness. Postmortem high-resolution scanning transmission electron microscopy (HRSTEM) combined with electron energy loss spectroscopy (EELS) of film surfaces shows a strong surface depletion of Mn for PCMO, leading to a 2–3 nm thick Pr-enriched surface. Emerging small peaks in XRD after 1 h of electrolysis are consistent with a thin cubic PrO$_{2+x}$ layer. In contrast, the Mn concentration at the LSMO surface is only slightly reduced.

Surface termination of the manganite films in H$_2$O. The study of surface termination of epitaxial perovskite films using environmental high-resolution transmission electron microscopy (ETEM) was demonstrated by Roddatis et al.[42] and requires careful TEM lamella preparation, as documented in the Supplementary Figs. 8–11 and the associated text. The changes of

surface termination of the LSMO and PCMO (001) oriented thin film electrodes in high vacuum (HV), O$_2$ and H$_2$O are shown in Fig. 2. For LSMO predominant A-terminated surfaces (La–Sr–O) are observed in O$_2$, whereas in high vacuum (HV), a mixed surface termination with disorder at the B-terminated (Mn–O) areas is developed. This is observed even after saturation of the surface in 1 mbar O$_2$. In H$_2$O vapor, the LSMO surface appears to be dominated by an A-site layer; however, Mn is still present as dynamic surface adatoms. For PCMO, a disordered surface develops in HV following the ordering of the surface in 1 mbar of O$_2$, where a mixed termination of an ordered surface is observed. In H$_2$O, a mixed surface termination emerges, where the A-terminated areas (Pr–Ca–O) show higher ordering compared to the B-terminated areas. Surface Mn adatoms as well as subsurface lattice Mn is highly mobile.

The determination of surface termination requires the comparison of the HRTEM images with simulated images (Fig. 2d, h). In these simulations, the lamella thickness t at the surface is estimated from measurement of the inelastic scattering intensity by EELS and fine-tuned by a fit of contrast of simulated to experimental images using a Monte–Carlo-based simulated least-squares optimization, yielding $t = 4.2$ (4.3) nm for LSMO (PCMO). The obtained electron optical parameters, such as defocus, spherical aberration, astigmatism, and axial coma, fit reasonably well to those estimated from tilt-tableau measurements via the Cs-corrector software. The different surface terminations can be clearly distinguished by the weaker contrast of the MnO columns. In the subsurface, A-site and B-site columns are separable from contrast due to different atomic numbers and octahedral tilt patterns of MnO$_6$ octahedra. Details of the image fitting and parameters used can be found in the Supplementary Fig. 12 and Supplementary Table 1.

Reversible Mn-adatom dynamics at the LSMO–H$_2$O interface. Figure 3 shows a time sequence of HRTEM images for the LSMO x = 0.4 (001) surface in 0.5 Pa of H$_2$O. The full image series is compiled in Movie M01. The surface is well ordered and shows stable A-termination over more than 30 min. However, mobile Mn is, in fact, present on the surface. This is indicated by the sudden appearance and disappearance of atom contrast at B-layer surface positions on flat stable A layers (Fig. 3a). We define the detection limit of Mn atoms by the amplitude of the signal above the noise level 3σ, where σ is the standard deviation of the background fluctuations of the CCD signal at an area above the surface in the presence of the experimental gas. Image simulation and contrast quantification show that signal to noise ratio at the used frame rate of 4.4 fps does allow for detection of triple or higher occupancy of B-columns by Mn at a 4.2-nm thick lamella surface (Fig. 3b, c).

Closer inspection of image contrast in Fig. 3a reveal adatom contrast mainly appears at interstitial surface positions and rarely at the nominal octahedral positions of an ideal non-reconstructed surface. Contrast quantification of the columns of Mn adatoms is obtained by calibration of the experimental A-site contrast at the lamella surface to the simulated contrast, as shown in the Supplementary Figs. 13–15. Based on contrast simulations, the interpretation of dynamic adatom contrast other than Mn on a static A-layer is unlikely: O and OH species are below the contrast detection limit. La/Sr occupancy on B-terminated layers can be excluded from contrast. Fast La/Sr adatom dynamics on a stable A-terminated layer can be not entirely excluded from contrast. However, this would lead to an A-enriched surface with a Mn depleted layer, which is contrary to our observations for LSMO but in agreement to Mn surface leaching in PCMO reported below. Since all experiments in different environments

3
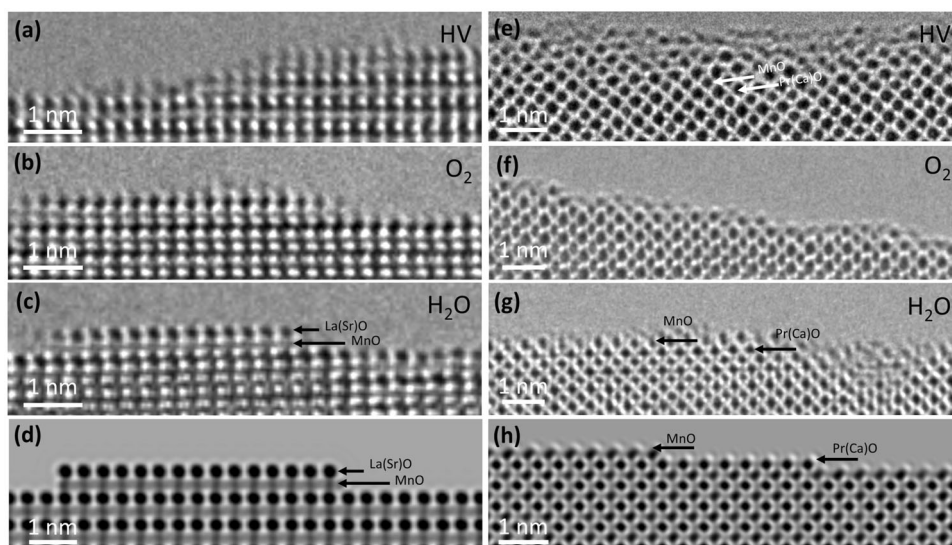
Fig. 2 HRTEM cross plane images of LSMO and PCMO (001) surfaces in different ambients. All images are taken at negative defocus, i.e., atomic columns appear as dark contrast, and with objective lens aberrations corrected up to 5th order. **a–d** LSMO is imaged in the pseudocubic [110] zone axis. **a** Mixed B- and A- termination in high vacuum (HV). **b** Dominant A-termination in 1 mbar O_2. **c** In 0.5 Pa H_2O, the surface consists of a stable A-layer with highly mobile Mn on top (see Fig. 3). **d** Simulated image with A-termination and surface step. **e–h** PCMO is imaged in the orthorhombic [110] zone axis. **e** Disordered surface structure in HV. **f** Highly ordered surface in 1 mbar of O_2 with a mixed termination. **g** In 0.5 Pa of H_2O, the B-terminated areas of PCMO exhibit pronounced disorder with mobile Mn. **h** Simulated image for PCMO with different surface terminations.
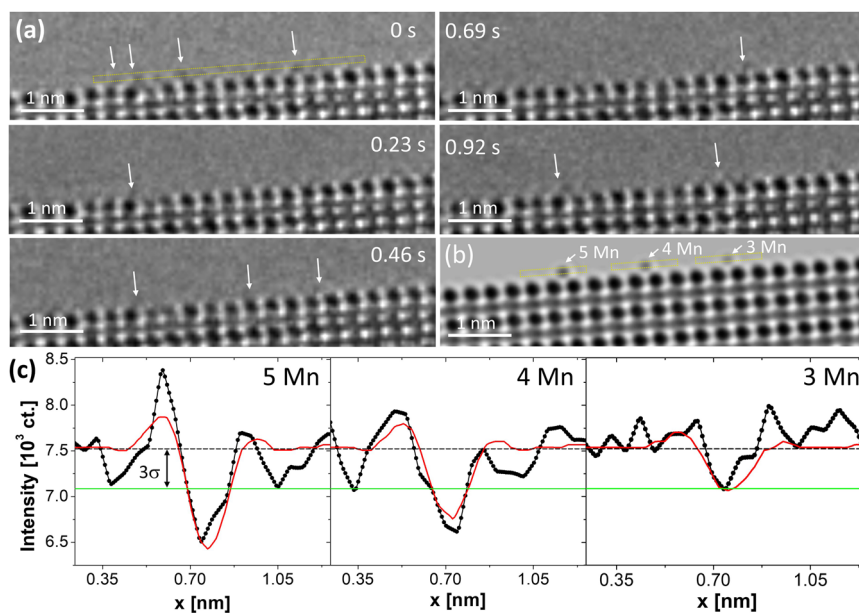

Fig. 3 Observation of dynamic Mn adatoms on a LSMO (001) surface in 0.5 Pa of H_2O at [110] zone axis. a Time sequence of HRTEM images taken at 4.4 fps at negative defocus. Mn-adatom contrast appears and disappears on a stable La(Sr)O surface layer as indicated by white arrows. **b** Simulated HRTEM image with Mn-adatom column occupation of 3, 4, and 5. The Mn columns are located at interstitial surface positions on an A-terminated sample. Lamella thickness is 4.2 nm. **c** Line profiles of simulated (red) and experimental (black with symbols) images of B-columns with 3, 4, and 5 Mn atom occupation. The 3σ threshold indicates the detection limit of Mn columns above noise level, i.e., triple Mn occupation at a B-layer column. The time sequence gives a lower limit of the Mn-adatom hopping rate of $r \geq 4\,s^{-1}$.

reveal that surface Mn is more mobile than A-type cations, our overall conclusion from image contrast and electrochemical behavior is that Mn adatoms are the highly mobile species on stable LSMO surfaces in H_2O.

The camera frame rate of around 4 fps is selected as a compromise between achieving sufficient signal to noise ratio and capturing some of the surface dynamics. Double Mn B-layer occupancy corresponds to the detection limit at 3σ of the noise level. Both triple Mn as well as higher Mn B-layer occupancy

contrast appears and disappears with the frame rate used. We can thus only determine a lower limit of the surface hopping rate, which is given by the frame rate of the images. If triple Mn occupation appears and disappears on the timescale of the frame rate, it may be attributed to one of the following events: (i) A single Mn atom hops to another site and the remaining double occupation contrast becomes invisible. (ii) Two or three Mn atoms coincidentally hop to another site and the B-site contrast on the original site disappears. Since (ii) has a lower probability
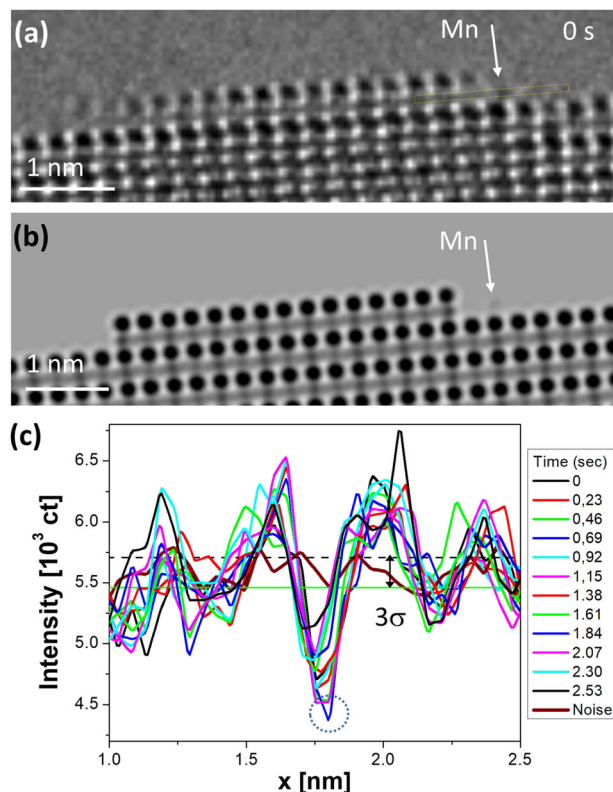
Fig. 4 Slowed down Mn surface mobility due to a unit cell height surface step at a LSMO (001) facet in 0.5 Pa of H₂O. a First HRTEM image of a time sequence taken at a frame rate of 4.4 fps with the surface step taken at the same conditions as in Fig. 3; see Movie M02. **b** Simulated HRTEM image with the step and 3 Mn occupation contrast on a slightly displaced B-site column. **c** Line profiles of the time sequence taken at the B-layer as indicated by the green box in **a**. It is showing an increased sticking time of a triple Mn column of 1.4 s near the step edge compared to ≤0.23 s at the flat surface, providing evidence for a locally increased surface barrier.

than (i) and represents the slowest process, it defines the minimum detectable hopping rate of $r \geq 4\,\text{s}^{-1}$.

The dynamic state with highly mobile Mn atoms on top of a more or less static A-terminated layer can be strongly affected by the presence of a surface step. Since the Mn surface mobility depends on the surface activation barrier, it can be strongly reduced at step edges due to an Erich–Schwöbel barrier. Figure 4 shows an increased contrast of mobile Mn atoms in the vicinity of step edges formed by a static A-terminated layer. The reduction of Mn mobility in the vicinity of the step edges can directly be observed in the Movie M02. The analysis of line profiles at the B-layer location in the vicinity of the step edge in Fig. 4 reveal a reduction of the Mn-adatom hopping rate from $r \geq 4\,\text{s}^{-1}$ to $r \approx 0.7\,\text{s}^{-1}$. Remarkably, the A-layer forming the step edge in Fig. 4 is quite stable and does not change on the timescale of the Movie M02 of 1 min 25; see also Supplementary Fig. 16.

Compared to H₂O, the Mn surface mobility on LSMO (001) in high vacuum (HV) and in other gases is strongly reduced at the same dose rate (Supplementary Figs. 17–19, Movies M03–M05). The surface with mixed termination shows contrast changes on the B-site columns with $r \leq 0.25\,\text{s}^{-1}$ in HV and $r \leq 0.2\,\text{s}^{-1}$ in 100 Pa O₂, where the highly ordered surface is predominantly A-site terminated. The high Mn surface mobility on LSMO (001) is thus a unique observation in H₂O and is visible in a pressure range of 0.01–5 Pa. At higher H₂O pressures, LSMO becomes unstable, possibly due to the impact of ions formed by beam-induced

ionization of H₂O. Despite the high mobility, the Mn leaching is rather slow, as confirmed by the post-ETEM stoichiometry analysis (Supplementary Fig. 20). Furthermore, the Mn valence state remains quite stable, indicating only a slight Mn reduction in increasing H₂O pressure and ruling out pronounced formation of oxygen vacancies.

Irreversible Mn-adatom dynamics at the PCMO–H₂O interface. Figure 5 shows a time series of HRTEM images of the (001) PCMO surface in 0.5 Pa H₂O, taken from Movie M06. After fully ordering in O₂ (Fig. 2f), the addition of H₂O causes the surface to form a disordered layer of highly mobile Mn atoms, visible as rapid fluctuation of B-site contrast. Similar to LSMO, the hopping rate of Mn atoms is above the frame rate of the camera, i.e., $r \leq 4\,\text{s}^{-1}$. In contrast to the disordered B-terminated surface, the A-subsurface layer remains highly ordered and static on the timescale of several seconds (Movie M06). In addition, an increase of contrast dynamics is observed at the B-site columns at the subsurface. Figure 5b, c shows the later stages of the PCMO (001) surface in 0.5 Pa H₂O. Three min after initiation, the fast Mn leaching has led to the formation of a Pr-rich surface bilayer (Movie M06) which further grows up to a thickness of 3–4 monolayers over the course of the in situ experiment (11 min). The growth of a cubic phase due to Mn leaching is directly visible in the surface structure. Postmortem EELS analysis of the surface area in Fig. 5f reveals Pr and O, whereas the Mn L-edge at 640 eV as well as Ca L-edge at 346 eV (not shown) are below the noise level. We thus associate the cubic oxide visible in HRTEM with PrOₓ, with x close to 2. The growth speed of the PrOₓ slows down over time, indicating self-passivation of the surface by the formed PrOₓ layer. Post-ETEM EELS of the Mn L and O K edges at the PCMO surface region reveals a pronounced Mn depletion (Supplementary Fig. 21), which is accompanied by Mn reduction. Leaching out of subsurface Mn in PCMO (001) is only observed in H₂O and is absent in HV (Movie M07) and O₂ (Movie M08). In contrast, the Mn concentration at LSMO surfaces remains unmodified. This is fully consistent with the observation of different electrode behavior in electrochemical experiments described above.

Enhanced Mn mobility at (001) surface due to presence of adsorbed H₂O layer. The formation of a few monolayer thick water layer on oxide surfaces down to pressures of ~10^{-5} Pa much below the equilibrium vapor pressure of water of $p_{vap} = 3.17$ kPa at T = 25 °C has been previously demonstrated[50–52]. It is driven by the large adsorption enthalpy of H₂O on oxide surfaces of the order of $\Delta H_{ad,ox}$—160 kJ/mol[51,53]. Although this value might vary between different oxides, $\Delta H_{ad,ox} < \Delta H_{ad} = -44$ kJ/mol for H₂O on bulk water reflects exothermic water adsorption on oxide surface at much reduced pressures. In the HV of the ETEM ($p \geq 10^{-5}$ Pa), the effect of H₂O condensation on manganite surfaces can be only avoided by using a cold trap that is reducing the partial pressure of H₂O in HV by one order of magnitude[42]. The thickness of the adsorbed water layer in the ETEM experiments as a function of p_{H_2O} is calculated by using the energy balance between surface energy γ_s of the oxide in HV, the surface energy γ_{H_2O} of liquid H₂O to vapor and ΔH_{ad} (see Supplementary Fig. 22 and associated text). The liquid state of 2–4 monolayer H₂O is consistent with our observation of enhanced mobility of Mn on manganite (001) surfaces in a pressure range between 0.01 and 5 Pa of H₂O compared to HV.

Thermally induced versus electron beam-induced hopping. In order to separate out the effect of the electron beam on adatom motion from the thermally induced motion, the momentum
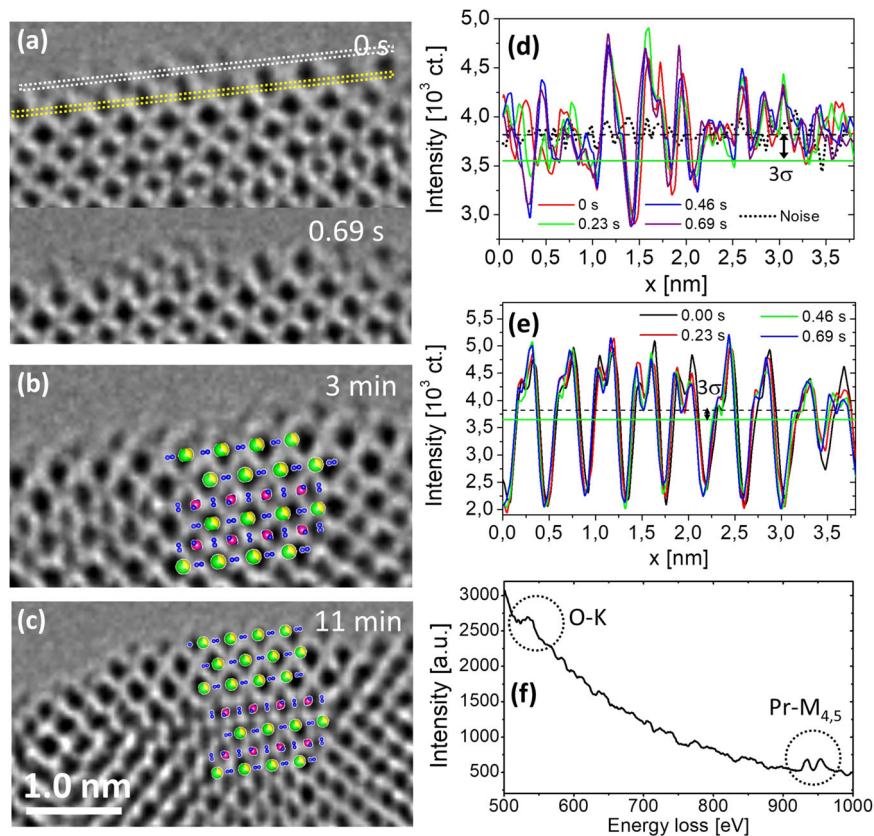
Fig. 5 Atomic surface dynamics of the PCMO (001) surface in 0.5 Pa H_2O. a HRTEM images taken from a time series taken at a rate of 4 fps at [110] zone axis and negative defocus, compiled in Movie M06. **b**, **c** Later stages of that surface area at same conditions. The line profiles are taken at the B-site (**d**) and A-site (**e**) columns. Whereas the A-site columns of the first subsurface layer remain ordered (**f**), the B-site columns transform into a dynamical highly disordered surface structure. The measured hopping rate of Mn adatoms is $r \geq 4\,s^{-1}$, from triple Mn coincidence occupation. In addition to surface movement, there is a pronounced leaching of Mn from the subsurface to the surface leading to the growth of a Pr-rich surface layer, where Mn $L_{3,2}$ is below the detection limit (**f**).

transfer from scattering of the high energy primary electron beam on the adatoms is calculated. As pointed out by Egerton[54], for energies of primary electrons $E_0 \geq 10\,keV$, the interaction is dominated by elastic scattering of the incident electrons at the atomic nuclei, and momentum transfer due to inelastic scattering at the electron shell can be disregarded. This allows calculation of the momentum transfer using the Rutherford scattering equation. We consider the maximum momentum transfer perpendicular to the primary electron beam, which gives rise to transversal movement of adatoms on a surface parallel to the electron beam. Figure 6 compares the beam-induced hopping rates for O, Mn, Sr and La adatoms to the thermally activated hopping rate as a function of the surface activation energy E_a for an upper limit of used dose rates of 12.000 $e^-/\text{Å}^2 s$ (see method section). For $E_a \geq 0.2\,eV$, the calculated beam-induced hopping rate for Mn adatoms is below the experimentally observed hopping rate in HV, indicating that the slow Mn motion is thermally activated. The comparison of the calculated thermally activated hopping with the experimentally observed r (HV) $\approx 0.25\,s^{-1}$ leads to an estimated E_a (Mn) $\approx 0.75\,eV$ in HV. The increase of the Mn-adatom hopping in H_2O to r (H_2O) $\geq 4\,s^{-1}$ thus can be interpreted as resulting from a reduction of the effective surface activation barrier in the presence of a H_2O layer to E_a (Mn) $< 0.62\,eV$ most probably due to partial solvation of surface Mn in H_2O. Furthermore, the calculation of momentum transfer between the electron beam and H_2O shows that the adsorbed H_2O layer is only marginally affected by the beam since the beam-induced desorption rate is with $\approx 2.5\,10^{-3}\,s^{-1}$ orders of magnitudes below

the impingement rate of H_2O molecules of around $10^3\,s^{-1}$ at $p = 0.5\,Pa$.

Parallel trends in electrolysis and ETEM studies with respect to reversible and irreversible dynamics. For LSMO $x = 0.4$, the (001) interface to liquid H_2O is quite stable both in in situ ETEM experiments as well as in cyclovoltammetry in alkaline conditions between $+1.1$ and $1.75\,V$ vers. RHE. Only slow Mn leaching is observed in previous studies by postmortem XPS after 1 h of electrochemical OER, which can be further slowed down by choosing a Mn/A ratio ≥ 1 ref. [55]. In contrast to LSMO, the in situ ETEM study of PCMO shows pronounced irreversible surface dynamics of Mn, leaching into the liquid H_2O layer in parallel to fast drop of OER activity in electrolysis and observation of a Pr-rich surface layer in postmortem studies. The huge difference in reversibility of Mn-adatom motion at the interface between the more or less static A-site terminated layer and liquid H_2O must therefore be attributed to the different materials properties of LSMO and PCMO. Post-ETEM electron energy loss spectroscopy (EELS) of the Mn L edge at a ≈ 1-nm thick surface layer on PCMO demonstrates a change of Mn valence from 3.5 ± 0.1 after oxidation in O_2 to 3.2 ± 0.1 after ETEM study in 0.5 Pa and 3.1 ± 0.1 in 5 Pa of H_2O (Supplementary Fig. 21). Thus, Mn is reduced although the experiments are performed under anodic polarization. In contrast, for LSMO the pristine Mn valence of 3.5 ± 0.1 after oxidation in O_2 and 3.4 ± 0.1 after ETEM study in 0.5 Pa H_2O is preserved within the error of measurements (Supplementary Fig. 20). Previous post electrochemical XPS studies of
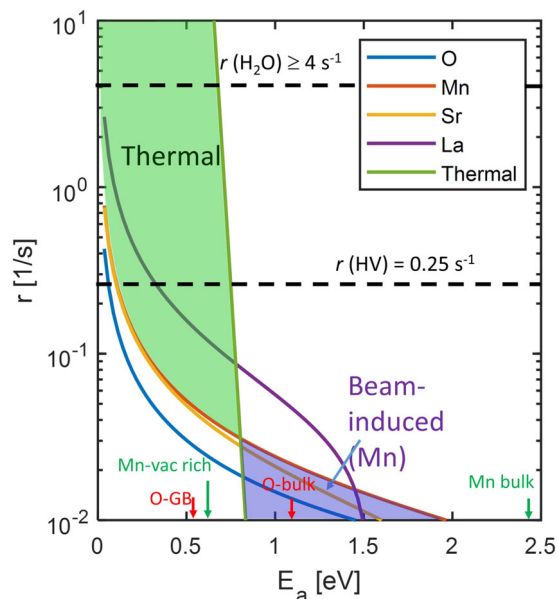
Fig. 6 Calculated beam-induced and thermally activated adatom hopping rate r at T = 22 °C as a function of the surface activation energy E_a. Additionally, the experimentally observed Mn-adatom hopping rates in high vacuum r(HV) and r(H$_2$O) in 0.5 Pa H$_2$O are indicated. Colored areas mark the regimes for thermally and beam-induced hopping for Mn. The activation energy of O diffusion in bulk LMO is from ref. [65] and for O in Sr-doped LMO grain boundaries from ref. [66]. For the activation energy of Mn the lower and upper limit of Mn diffusion in LMO are indicated, since it shows a broad range of values, depending on the La-off-stochiometry of the sample[67]. See method section for details of the calculations.
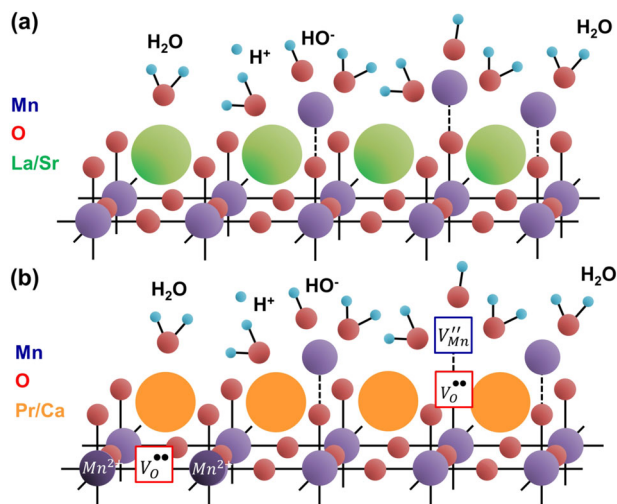
Fig. 7 Schematic representation of a snapshot of the dynamic manganite-H$_2$O interface. a For LSMO, the observed reversible Mn-adatom dynamics in liquid H$_2$O is connected to the absence of defect reactions and preservation of Mn oxidation state. **b** In contrast for PCMO, the reduced Mn^{2+} species are formed, due to surface and subsurface oxygen vacancy $V_O^{\cdot\cdot}$ formation.

LSMO (001) do not show surface loss of oxygen[29]. As summarized in Fig. 7, these observations suggest that stabilization of high oxidation states of surface Mn is essential for a high reversibility of Mn-adatom movement and thus for the stability on the surface. Surface reduction and Mn^{2+} formation lead to irreversible Mn surface dynamics due to the higher solubility of Mn^{2+} in

H$_2$O compared to Mn^{3+}. Leaching of Mn^{2+} in H$_2$O is also predicted by a Pourbaix diagram of binary Mn–O compounds.

We attribute the different behavior of LSMO and PCMO to their different electronic properties, in particular covalency and charge localization (see Supplementary Figs. 23 and 24). Metallic LSMO exhibits spatially delocalized charge carriers, so called large polarons due to a larger Mn–O covalency and an electron-phonon coupling constant $\alpha \approx 1$[56]. As long as the metallic state is preserved at the electrode surface, an extra charge acquired from water oxidation cannot change the valence state of a single atomic surface species. In contrast, PCMO x = 0.33 displays localized charge carriers, so called small polarons due a smaller Mn–O covalency and larger $\alpha \approx 3$ (see ref. [57]). They represent Zener polarons, which are located on Mn–O–Mn bridges[58–60]. From the chemical perspective, such a Zener polaron represents the formation of an O-oxo species, due to the presence of a localized hole charge and thus the oxidation of the lattice oxygen with a formal valence state of O^{2-}. Under anodic polarisation, hole type polarons can accumulate on the surface near Mn–O–Mn bridges and thus can easily induce oxidation of lattice oxygen to O$^-$ as an intermediate step for subsequent formation of vacancies V_O. Formation of O$^-$ and V_O thus can therefore reduce Mn and turn reversible adatom dynamics of oxidized metal species into irreversible processes of reduced metal species. Note that the different charge carriers may be also the origin of the different Tafel slopes b of both manganites. For LSMO, $b \approx 60$ mV/dec fits to the theoretical prediction for a chemical rate-limiting step that follows an electrochemical pre-equilibrium, probably O–O bond formation. For PCMO, the higher $b \approx 90$–120 mV/dec is consistent with electron transfer as the rate-limiting step and thus may reflect the lower intrinsic electric conductivity as well as limitations due to surface reduction.

Solvated dynamic Mn adatoms and impact on reaction mechanisms of oxygen evolution. The demonstrated parallel trends in in situ ETEM and electrolysis studies underpins that the observation of enhanced surface dynamics of Mn adatoms in H$_2$O is highly relevant for the real-world electrochemical behavior of the manganite electrodes. Clearly, there are differences in the properties of a Helmholtz layer in a liquid electrolyte with ion concentration of 10^{-1} M and the thin water layer adsorbed on top of oxide materials in ETEM. In particular, the ion concentration is much lower, with typically 10^{-6}–10^{-7} M in the vapor[45] that is close to the ion concentration at neutral pH. However, the composition of ions generated by electron impact is different since positively charged ions such as H$_2$O$^+$ dominate over anions such as OH$^-$. Our ETEM studies are performed under positive electric potentials of U = +2 V with respect to ground and thus under anodic polarization. Due to the high electric conductivity of the manganite lamella on highly conductive Nb-doped SrTiO$_3$, beam-induced potentials can be disregarded[45]. The comparison of hopping rates in different ambients clearly demonstrate that the observed ≥20× increased Mn-adatom mobility in H$_2$O while other conditions of the experiment remain the same is not due to the electron beam. This is fully understandable from the calculation of beam-induced momentum transfer in Fig. 6. Therefore, the enhancement of thermally activated adatom motion in water is fully relevant for OER catalysis in ex situ electrochemical conditions. It can be attributed to a partial solvation of surface Mn in liquid H$_2$O. Such solvation effects thus do not only affect the adsorption energies of the reactants but also strongly modify the coordination and electronic properties of active sites.

The formation of a partial solvation shell of H$_2$O around chemisorbed Mn adatoms in OER thus has far-reaching consequences for understanding of the reaction pathways. First

of all, Mn can develop other, more flexible coordination to OH_2 and OH compared to a static octahedral Mn–O coordination of a frozen surface (Fig. 7). This would allow new configuration for the formation of the O–O double bond. Furthermore, the question is raised whether the Mn dynamics affect the OER. The electron transfer rate per surface Mn atom derived from RRDE measurements is between $0.2\,s^{-1}$ (1.6 V) and $10\,s^{-1}$ (1.74 V vers RHE), assuming a Faraday efficiency of 1 and a complete Mn surface coverage. Due to partial coverage, these numbers represent a lower limit of the electron transfer rate per Mn. Comparing these numbers with the observed lower limit of Mn-adatom hopping $r \approx 4\,s^{-1}$, shows that both are of the same order of magnitude or even higher. Consequently, Mn can move over several surface sites during a full O_2 evolution cycle.

In summary, our study reveals unexpectedly high Mn-adatom hoping rates implying that the understanding of OER mechanisms requires theoretical treatment beyond the frozen surface approximation. There is strong experimental evidence from ref. [21] that surface Mn species represent the catalytically active sites for LSMO. Fast Mn leaching at PCMO surfaces dramatically decreases OER activity. Although hopping rates and contrast of single Mn atoms are beyond the resolution of our experiments, the observation of dynamic multiple occupancy of surface sites by Mn moieties establishes a pronounced dynamical surface reconstruction of the catalyst-water interface with partial solvation of surface Mn atoms in H_2O. Mn-adatom contrast dominantly appears at interstitial surface sites rather than the nominal octahedral B sites of an unreconstructed ideal surface, suggesting a modified surface coordination. The implications of these findings are quite far-reaching. First of all, leaching of reduced transition metal species is observed for many transition metal oxides[61,62]. Our results imply that the underlying transition from reversible dynamics of surface atoms to irreversible leaching of surface and subsurface metal species is controlled by charge localization and a related shift of the Fermi energy. Indeed, the recent results on self-gating of electrocatalysts evidences a modification of the Fermi level at the onset of an electrochemical reaction[63]. The finding of pronounced reversible dynamics of partially solvated adatoms in the stationary state of OER implies that for the theoretical understanding of heterogenous catalysis some aspects of homogeneous catalysis must be taken into account, such as modified metal coordination, different valence states, solvation shell reorganization during electron transfer, solvent thermal fluctuations and possibly Mn displacements during intermediate formation. Incorporating these effects into theoretical analysis will open new strategies of breaking scaling relations between adsorption energies and thus new perspectives in atomic scale design of efficient and stable electrode surfaces for OER.

Methods

Film fabrication and structure. $La_{0.6}Sr_{0.4}MnO_3$ and $Pr_{0.33}Ca_{0.67}MnO_3$ (001) films were prepared by ion-beam sputtering (IBS) on 0.5 wt% Nb-doped $SrTiO_3$ (STNO) substrates with (100)-orientation (CrysTec GmbH, Berlin, Germany). The $La_{0.6}Sr_{0.4}MnO_3$ ($Pr_{0.33}Ca_{0.67}MnO_3$) with thickness of 80 nm were grown at 800 °C (650 °C) in an oxygen atmosphere of $1.7 \cdot 10^{-4}$ mbar. In order to avoid rectifying junction properties for PCMO, a 20-nm thick $La_{0.6}Sr_{0.4}MnO_3$ (LSMO) buffer layer was deposited without vacuum breaking. LSMO has a rhombohedral lattice, spacegroup R$\bar{3}$c with a small rhombohedral tilt angle of 90.37°, lattice parameter $a = 5.47$ Å, which converts in a pseudocubic lattice constant $a_c = 3.87$ Å. PCMO is orthorhombic, spacegroup Pbnm, with ideal lattice parameters $a = 5.42$ Å, $b = 5.45$ Å and $c = 7.67$ Å. Due to the larger lattice constant of STNO ($a = 3.92$), the films have in-plane tensile and out of plane compressive strain leading to $a_c = 3.83$ Å (LSMO) and $c = 7.62$ Å (PCMO). For LSMO, we use pseudocubic notation to facilitate the comparison of the (001) surface with the equivalent (001) surface of PCMO. The films show atomically flat surfaces with unit cell high steps. The temperature dependent electric resistivity of the films shows the expected metal-like (LSMO) and small polaron hopping like (PCMO) characteristics. See Supplementary Figs. 4–7 and 24 for more details.

Backside contacts for the STNO substrate consisted of 5 nm Ti and 100 nm Pt layers prepared by IBS at room temperature to ensure an ohmic contact. Carbon tape and InGa eutectic (Sigma–Aldrich, Munich, Germany, 99.99%) served as the flexible and adjustable conductive spacer. In the final assembly, only the thin film surface is exposed to the electrolyte after fixation with chemically stable, nonconductive epoxy (Omegabond 101).

Electrochemistry. The electrochemical measurements were carried out with two Interface 1000E potentiostats (Gamry Instruments Inc., Warminster, PA, USA) in a bipotentiostat setup and an RRDE-3A rotator (ALS Co. Ltd., Tokyo, Japan). The rotating ring electrode consists of a disk electrode of the assembled PCMO|LSMO| NSTO electrode with a diameter of 4 mm and a Pt ring electrode with an inner diameter of 5 mm and an outer diameter of 7 mm. All electrochemical measurements were performed in 0.1 M KOH electrolyte prepared by diluting KOH stock solution (Sigma–Aldrich, Munich, Germany) with deionized water (MilliQ, >16.5 MΩ). The electrolyte was saturated with Ar gas at least 30 min before measurements and continuously purged with Ar throughout the measurement. Electrode potentials were converted to the reversible hydrogen electrode (RHE) scale using $E_{RHE} = E_{applied} + E_{ref}$, where $E_{ref} = 0.993$ V vs. SCE was obtained from the hydrogen evolution using a clean Pt disk. Cyclovoltagramms are measured at 10 mV/s with rotation of 1600 turns per minute. In Fig. 1b, between third and 4th cycle, chronoamperometric OER is measured at 1.5, 1.55, 1.6, 1.65, 1.7, 1.75, and 1.8 V vs RHE, each 60 s.

Environmental TEM experiments. Transmission Electron Microscopy (TEM) experiments were carried out using a FEI Titan ETEM G2 80–300, operated at 300 kV. The microscope is equipped with a Cs-corrector of the image forming lens for enhanced high-resolution TEM (HRTEM) imaging, and a Gatan Image Filter (GIF) Quantum 965ER. A Gatan UltraScan 1000XP CCD was used to collect all movies with rate of about 4 frames per second (fps) in 512 × 512 pixels. The microscope was used in the high vacuum (HV) mode ($\sim10^{-5}$ Pa) with cold trap to reduce H_2O partial pressure, as well as in environmental mode using H_2O, O_2 and He in a pressure range between 0.01 and 100 Pa. The following movies are provided: M01 LSMO 0.5 Pa H_2O flat facet, M02 LSMO 0.5 Pa H_2O Schwoebel Barrier, M03 LSMO HV, M04 LSMO 0.5 Pa O_2, M05 LSMO 0.5 Pa N_2, M06 PCMO 0.5 Pa H_2O, M07 PCMO HV, M08 PCMO 0.5 Pa O_2, M09 LSMO 10 Pa O_2 recrystallization early state and M10 LSMO 10 Pa O_2 recrystallization late state. All time resolved HRTEM experiments were performed at a beam current of 4 nA and beam radius between 80 and 100 nm, resulting in a spatially in homogeneous electron dose rate of 8000–12,000 e/Å^{-2}s. Local electron dose rates at the location of TEM lamella surfaces are measured by calibrated CCD contrast with 0.136 electrons/ counts, yielding $\sim$10,000 e/Å^{-2}s for the adatom hopping studies. This dose rate is two orders of magnitude below the damage threshold in HV. Imaging over a time of 10 min keeps the total electron dose ≤6 10^3 As/cm^2, where no changes by electron irradiation are observed in HV, in good agreement with the studies of the intrinsic surface in ref. [41].

Electron energy loss spectroscopy (EELS). Was performed using Gatan Quantum 965ER post-column energy filter in the same FEI Titan ETEM. Spectra of the Mn L, O K, and Pr M edges were acquired. For analysis of the Mn L edge spectra, Hartree–Slater (HS) type cross-section functions from Gatan's Digital Micrograph are used. The Mn valence state has been acquired from a C++ based LabTalk script using OriginLab software. EEL spectra are extracted from spectrum images at an area of vacuum and at different H_2O vapor pressure for postmortem analysis. Power-law background functions are fitted to a 50 eV wide window before each Mn L-edge and 25 eV for O K-edge for background subtraction. By using dual EELS acquisition, the ZLP is used to correct the drift of the energy shift.

TEM lamella preparation. TEM lamellae were prepared from epitaxially grown (001) oriented thin films by Focused Ion-Beam lift-out technique using a noble metal free protection layer and careful low energy ion milling for the preparation of ultrathin lamella with a thickness close to the surface between 4 and 10 nm. The loss of oxygen by Ar milling is compensated by a treatment in pure oxygen. Further details are described in the Supplementary information and Movies M09-M10.

Image simulations. Atomic models and the high-resolution TEM simulated images were calculated using the multislice method as established in the QSTEM package[64], where electron optical parameters were optimized by using a metropolis algorithm implementation to fit simulated to experimental images. Structure models for the image simulations are based on the Pbnm spacegroup for PCMO with lattice parameters $a = 5.42$ Å, $b = 5.45$ Å and $c = 7.67$ Å and R$\bar{3}$'c for LSMO using $a_c = 3.87$ Å. Details and parameters used for image simulation are given in the SI.

Calculation of electron beam-induced and thermally activated hopping. Using the analytical solution given in ref. [54], the adatom hopping rate is

$$R = \frac{J}{e}\frac{\sigma_0}{4}FZ^2\left[\frac{1}{\sin^2(\vartheta_{min}/2)} - \frac{1}{\sin^2(\vartheta_{max}/2)}\right] \qquad (1)$$

where ϑ is the scattering angle of the electrons. The limits

$$\vartheta_{min} = \arcsin\left[2\left(\frac{E_s}{E_{max}}\right)^{0.5}\right] \text{ and } \vartheta_{max} = \pi - \arcsin\left[2\left(\frac{E_s}{E_{max}}\right)^{0.5}\right] \qquad (2)$$

are given by ratio of the captured surface energy E_s of the adatom to the maximum possible energy transfer E_{max}, which would correspond to a 180° scattering, i.e.,

$$E_{max}(eV) \approx \frac{1.1}{A}\left[2 + \frac{E_0}{511keV}\right]E_0(keV) \qquad (3)$$

A is the atomic mass, Z the nuclear charge, e the elementary electron charge, J is the current density of the primary electron beam, $\sigma_0 = 1$ barn $= 10^{-28}$ m^2 and $F = (1 - v^2/c^2)\left(\frac{v^4}{c^4}\right)$, where c is the velocity of light and v the velocity of the primary electrons. In order to calculate the hopping rate of an adatom on a surface, it is assumed that the kinetic energy transversal to the surface is equal to the surface activation energy E_a, i.e., $E_s = E_a$. In the Mn-adatom hopping studies, $E_0 = 300$ keV and for the current density an upper limit of the experimental values of $J = 2.0 \times 10^5$ A/m^2 is chosen, corresponding to 12,000 e/Å^{2}s.

The thermally activated hopping rate is given by

$$R_{th} = \nu_0 e^{\frac{-E_a}{k_B T}} \qquad (4)$$

with adatom vibration frequency ν_0 and Boltzmann constant k_B. We have chosen $\nu_0 = 10^{12}$ s^{-1}, which for $E_a = 0$ eV results in a thermal velocity for Mn atoms matching the maximum of the Maxwell–Boltzmann distribution.

Data availability

All relevant data are available from the corresponding authors on request.

References

1. Wiechen, M., Berends, H. M. & Kurz, P. Water oxidation catalysed by manganese compounds: from complexes to 'biomimetic rocks'. *Dalton Trans.* **41**, 21–31 (2012).
2. McCrory, C. C. L., Jung, S., Peters, J. C. & Jaramillo, T. F. Benchmarking heterogeneous electrocatalysts for the oxygen evolution reaction. *J. Am. Chem. Soc.* **135**, 16977–16987 (2013).
3. Hong, W. T. et al. Toward the rational design of non-precious transition metal oxides for oxygen electrocatalysis. *Energy Environ. Sci.* **8**, 1404–1427 (2015).
4. Lyons, M. E. G. & Burke, L. D. Mechanism of oxygen reactions at porous oxide electrodes. Part 1.—oxygen evolution at RuO$_2$ and Ru$_x$Sn$_{1-x}$O$_2$ electrodes in alkaline solution under vigorous electrolysis conditions. *J. Chem. Soc. Faraday Trans. 1 Phys. Chem. Condens. Phases* **83**, 299–321 (1987).
5. Bockris, J. O'M. & Conway, B. E. Modern aspects series of chemistry. *Butterworths Sci. Publ. Lond.* **1**, 180 (1954).
6. Conway, B. E. & Salomon, M. Electrochemical reaction orders: applications to the hydrogen- and oxygen-evolution reactions. *Electrochim. Acta* **9**, 1599 (1964).
7. Lodi, G., Sivieri, E., De Battisti, A. & Trasatti, S. Ruthenium dioxide-based film electrodes—III. Effect of chemical composition and surface morphology on oxygen evolution in acid solutions. *J. Appl. Electrochem.* **8**, 135–143 (1978).
8. Kobussen, A. G. C. & Broers, G. H. J. The oxygen evolution on La$_{0.5}$Ba$_{0.5}$CoO$_3$. Theoretical impedance behaviour for a multi-step mechanism involving two adsorbates. *J. Electroanal. Chem.* **126**, 221–240 (1981).
9. Rossmeisl, J., Qu, Z. W., Zhu, H., Kroes, G. J. & Nørskov, J. K. Electrolysis of water on oxide surfaces. *J. Electroanal. Chem.* **607**, 83–89 (2007).
10. Wohlfahrt-Mehrens, M. & Heitbaum, J. Oxygen evolution on Ru and RuO$_2$ electrodes studied using isotope labelling and on-line mass spectrometry. *J. Electroanal. Chem.* **237**, 251–260 (1987).
11. Grimaud, A. et al. Double perovskites as a family of highly active catalysts for oxygen evolution in alkaline solution. *Nat. Commun.* **4**, 2439 (2013).
12. Rong, X., Parolin, J. & Kolpak, A. M. A fundamental relationship between reaction mechanism and stability in metal oxide catalysts for oxygen evolution. *ACS Catal* **6**, 1153–1158 (2016).
13. Mierwaldt, D. et al. In situ XANES/XPS investigation of doped manganese perovskite Catalysts. *Catalysts* **4**, 129–145 (2014).
14. Kuan-Yu Yeh & Michael J. Janik. In *Computational Catalysis* (ed. Aravind Asthagiri, M. J. J.) 116–156 (Royal Society of Chemistry, 2014).
15. Blakemore, J. D., Crabtree, R. H. & Brudvig, G. W. Molecular catalysts for water oxidation. *Chem. Rev.* **115**, 12974–13005 (2015).
16. Man, I. C. et al. Universality in oxygen evolution electrocatalysis on oxide surfaces. *ChemCatChem* **3**, 1159–1165 (2011).
17. She, Z. W. et al. Combining theory and experiment in electrocatalysis: insights into materials design. *Science* **355**, eaad4998 (2017).
18. Gono, P. & Pasquarello, A. Oxygen evolution reaction: bifunctional mechanism breaking the linear scaling relationship. *J. Chem. Phys.* **152**, 104712 (2020).
19. Calle-Vallejo, F., Krabbe, A. & García-Lastra, J. M. How covalence breaks adsorption-energy scaling relations and solvation restores them. *Chem. Sci.* **8**, 124–130 (2016).
20. Zhang, B. et al. Homogeneously dispersed multimetal oxygen-evolving catalysts. *Science* **352**, 333–337 (2016).
21. Arrigo, R. et al. In situ study of the gas-phase electrolysis of water on platinum by NAP-XPS. *Angew. Chem. Int. Ed.* **52**, 11660–11664 (2013).
22. Bergmann et al. Reversible amorphization and the catalytically active state of crystalline Co$_3$O$_4$ during oxygen evolution. *Nat. Commun.* **6**, 8625 (2015).
23. Risch, M. et al. Water oxidation by amorphous cobalt-based oxides: in situ tracking of redox transitions and mode of catalysis. *Energy Environ. Sci.* **8**, 661–674 (2015).
24. Xia, X. et al. On the role of surface diffusion in determining the shape or morphology of noble-metal nanocrystals. *Proc. Natl. Acad. Sci. USA* **110**, 6669–6673 (2013).
25. Chen, L. Y. & Ying, S. C. Adatoms on solid surfaces L. *Phys. Rev. B* **49**, 838–847 (1994).
26. Shiotari, A., Okuyama, H., Hatta, S., Aruga, T. & Hamada, I. Atomic-scale study of the formation of sodium-water complexes on Cu(110). *Phys. Chem. Chem. Phys.* **20**, 12210–12216 (2018).
27. Wang, Y. G., Mei, D., Glezakou, V. A., Li, J. & Rousseau, R. Dynamic formation of single-atom catalytic active sites on ceria-supported gold nanoparticles. *Nat. Commun.* **6**, 6511 (2015).
28. Raabe, S. et al. In situ electrochemical electron microscopy study of oxygen evolution activity of doped manganite perovskites. *Adv. Funct. Mater.* **22**, 3378–3388 (2012).
29. Scholz, J. et al. Rotating ring-disk electrode study of oxygen evolution at a perovskite surface: Correlating activity to manganese concentration. *J. Phys. Chem. C* **120**, 27746–27756 (2016).
30. Izgorodin, A., Winther-Jensen, O. & MacFarlane, D. R. On the stability of water oxidation catalysts: challenges and prospects. *Aust. J. Chem.* **65**, 638–642 (2012).
31. Kötz, R., Stucki, S., Scherson, D. & Kolb, D. M. In-situ identification of RuO$_4$ as the corrosion product during oxygen evolution on ruthenium in acid media. *J. Electroanal. Chem.* **172**, 211–219 (1984).
32. da Silva, G. C., Mayrhofer, K. J. J., Ticianelli, E. A. & Cherevko, S. Dissolution stability: the major challenge in the regenerative fuel cells bifunctional catalysis. *J. Electrochem. Soc.* **165**, F1376–F1384 (2018).
33. Stoerzinger, K. A. et al. The role of Ru redox in pH-dependent oxygen evolution on rutile ruthenium dioxide. *Surfaces. Chem* **2**, 668–675 (2017).
34. Cherevko, S. Stability and dissolution of electrocatalysts: building the bridge between model and "real world" systems. *Curr. Opin. Electrochem.* **8**, 118–125 (2018).
35. Kanan, M. W. & Nocera, D. G. In situ formation of an oxygen-evolving catalyst in neutral water containing phosphate and Co^{2+}. *Science* **321**, 1072–1075 (2008).
36. Handoko, A. D., Wei, F., Jenndy, Yeo, B. S. & Seh, Z. W. Understanding heterogeneous electrocatalytic carbon dioxide reduction through operando techniques. *Nat. Catal.* **1**, 922–934 (2018).
37. Kasian, O., Grote, J. P., Geiger, S., Cherevko, S. & Mayrhofer, K. J. J. The common intermediates of oxygen evolution and dissolution reactions during water electrolysis on iridium. *Angew. Chem. Int. Ed.* **57**, 2488–2491 (2018).
38. Yoshida, H. et al. Visualizing gas molecules interacting with supported nanoparticulate catalysts at reaction conditions. *Science* **335**, 317–319 (2012).
39. Lin, Y., Wu, Z., Wen, J., Poeppelmeier, K. R. & Marks, L. D. Imaging the atomic surface structures of CeO$_2$ nanoparticles. *Nano Lett.* **14**, 191–196 (2014).
40. Bugnet, M., Overbury, S. H., Wu, Z. L. & Epicier, T. Direct visualization and control of atomic mobility at {100} surfaces of Ceria in the environmental transmission electron microscope. *Nano Lett.* **17**, 7652–7658 (2017).
41. Kuwauchi, Y., Yoshida, H., Akita, T., Haruta, M. & Takeda, S. Intrinsic catalytic structure of gold nanoparticles supported on TiO$_2$. *Angew. Chem. Int. Ed.* **51**, 7729–7733 (2012).
42. Roddatis, V., Lole, G. & Jooss, C. In situ preparation of Pr$_{1-x}$Ca$_x$MnO$_3$ and La$_{1-x}$Sr$_x$MnO$_3$ catalysts surface for high-resolution environmental transmission electron microscopy. *Catalysts* **9**, 751 (2019).
43. Möbus, G. et al. Dynamics of polar surfaces on ceria nanoparticles observed in situ with single-atom resolution. *Adv. Funct. Mater.* **21**, 1971–1976 (2011).

44. Yuan, W. et al. Visualizing H_2O molecules reacting at TiO_2 active sites with transmission electron microscopy. *Science* **367**, 428–430 (2020).

45. Mildner, S. et al. Environmental TEM study of electron beam induced electrochemistry of $Pr_{0.64}Ca_{0.36}MnO_3$ catalysts for oxygen evolution. *J. Phys. Chem. C* **119**, 5301–5310 (2015).

46. Bakardjieva, S., Bezdička, P., Grygar, T. & Vorm, P. Reductive dissolution of microparticulate manganese oxides. *J. Solid State Electrochem.* **4**, 306 (2000).

47. Nemudry, A., Rudolf, P. & Schöllhorn, R. Topotactic electrochemical redox reactions of the defect perovskite $SrCoO_{2.5+x}$. *Chem. Mater.* **8**, 2232 (1996).

48. Köhler, L., Szabadics, L., Jooss, C. & Risch, M. Peroxide yield of the (001) $La_{0.6}Sr_{0.4}MnO_3$ surface as a bifunctional electrocatalyst for the oxygen reduction reaction and oxygen evolution reaction in alkaline media. *Batter. Supercaps* **2**, 364–372 (2019).

49. Stoerzinger, K. A., Qiao, L., Biegalski, M. D. & Shao-Horn, Y. Correction to "Orientation-Dependent Oxygen Evolution Activities of Rutile IrO_2 and RuO_2". *J. Phys. Chem. Lett.* **5**, 1636–1641 (2015).

50. Ketteler, G. et al. The nature of water nucleation sites on $TiO_2(110)$ surfaces revealed by ambient pressure X-ray photoelectron spectroscopy. *J. Phys. Chem. C* **111**, 8278–8282 (2007).

51. Srinivasan, S. G. et al. Crystal structures, surface stability, and water adsorption energies of La-Bastnäsite via density functional theory and experimental studies. *J. Phys. Chem. C* **120**, 16767–16781 (2016).

52. Opitz, A., Scherge, M., Ahmed, S. I. U. & Schaefer, J. A. A comparative investigation of thickness measurements of ultra-thin water films by scanning probe techniques. *J. Appl. Phys.* **101**, 064310 (2007).

53. Drazin, J. W. & Castro, R. H. R. Water adsorption microcalorimetry model: deciphering surface energies and water chemical potentials of nanocrystalline oxides. *J. Phys. Chem. C* **118**, 10131–10142 (2014).

54. Egerton, R. F. Beam-induced motion of adatoms in the transmission electron microscope. *Microsc. Microanal.* **19**, 479–486 (2013).

55. Scholz, J. et al. Tailoring the oxygen evolution activity and stability using defect chemistry. *Catalysts* **7**, 139 (2017).

56. Hartinger, C., Mayr, F., Loidl, A. & Kopp, T. Polaronic excitations in colossal magnetoresistance manganite films. *Phys. Rev. B Condens. Matter Mater. Phys.* **73**, 024408 (2006).

57. Hoffmann, J. et al. Effects of interaction and disorder on polarons in colossal resistance manganite $Pr_{0.68}Ca_{0.32}MnO_3$ thin films. *Mater. Res. Express* **1**, 046403 (2015).

58. Daoud-Aladine, A., Rodríguez-Carvajal, J., Pinsard-Gaudart, L., Fernández-Díaz, M. T. & Revcolevschi, A. Zener polaron ordering in half-doped manganites. *Phys. Rev. Lett.* **89**, 097205 (2002).

59. Jooss, C. et al. Polaron melting and ordering as key mechanisms for colossal resistance effects in manganites. *Proc. Natl Acad. Sci. USA* **104**, 13597 (2007).

60. Sotoudeh, M. et al. Electronic structure of $Pr_{1-x}Ca_xMnO_3$. *Phys. Rev. B* **95**, 235150 (2017).

61. Najafpour, M. M., Sedigh, D. J., Pashaei, B. & Nayeri, S. Water oxidation by nano-layered manganese oxides in the presence of cerium(iv) ammonium nitrate: important factors and a proposed self-repair mechanism. *N. J. Chem.* **37**, 2448 (2013).

62. Chivot, J., Mendoza, L., Mansour, C., Pauporté, T. & Cassir, M. New insight in the behaviour of $Co-H_2O$ system at 25–150 °C, based on revised Pourbaix diagrams. *Corros. Sci.* **50**, 62–69 (2008).

63. He, Y. et al. Self-gating in semiconductor electrocatalysis. *Nat. Mater.* **18**, 1098–1104 (2019).

64. Koch, C. *Determination of Core Structure Periodicity and Point Defect Along Dislocations*. Ph.D. Thesis, Arizona State University (2002).

65. Palcut, M., Wiik, K. & Grande, T. Cation self-diffusion and nonstoichiometry of lanthanum manganite studied by diffusion couple measurements. *J. Phys. Chem. C* **111**, 813–822 (2007).

66. Polfus, J. M., Yildiz, B. & Tuller, H. L. Origin of fast oxide ion diffusion along grain boundaries in Sr-doped $LaMnO_3$. *Phys. Chem. Chem. Phys.* **20**, 19142–19150 (2018).

67. Miyoshi, S. & Martin, M. B-Site cation diffusivity of Mn and Cr in perovskite-type $LaMnO_3$ with cation-deficit nonstoichiometry. *Phys. Chem. Chem. Phys.* **11**, 3063 (2009).

Author contributions

G.L. and V.R. carried out the ETEM experiments. T.M. and U.R contributed to image analysis. J.G. and G.W. did manganite epitaxy and structural analysis as well as electrochemical measurements. M.R. contributed to analysis of electrochemical data. L.R. provided software for image simulation. P.B. contributed to theoretical analysis of the results. C.J. did calculations on beam effects and water adsorption and wrote the manuscript. All authors commented on, discussed and edited the manuscript.

Competing interests

The authors declare no competing interests.

Additional information

Supplementary information is available for this paper at https://doi.org/10.1038/s43246-020-00070-6.

Correspondence and requests for materials should be addressed to C.J.

Reprints and permission information is available at http://www.nature.com/reprints

Publisher's note Springer Nature remains neutral with regard to jurisdictional claims in published maps and institutional affiliations.